1-1-2020

# Estimation of maize yield and effects of variable-rate nitrogen application using UAV-based RGB imagery

Meina Zhang
*Jiangsu Academy of Agricultural Sciences*

Jianfeng Zhou
*University of Missouri*, zhoujianf@missouri.edu

Kenneth A. Sudduth
*USDA Agricultural Research Service*

Newell R. Kitchen
*USDA Agricultural Research Service*

**ELSEVIER**

**Biosystems ENGINEERING**

## Research Paper

# Estimation of maize yield and effects of variable-rate nitrogen application using UAV-based RGB imagery

Check for updates

Meina Zhang [a,b], Jianfeng Zhou [b,*], Kenneth A. Sudduth [c], Newell R. Kitchen [c]

[a] Institute of Agricultural Facilities and Equipment, Jiangsu Academy of Agricultural Sciences, Nanjing, Jiangsu, 210014, China
[b] Division of Food Systems and Bioengineering, University of Missouri, Columbia, MO, 65211, USA
[c] Cropping Systems & Water Quality Research Unit, USDA-ARS, Columbia, MO, 65211, USA

## ARTICLE INFO

Accurate crop yield estimation is important for agronomic and economic decision-making. This study evaluated the performance of imagery data acquired using a unmanned aerial vehicle (UAV)-based imaging system for estimating yield of maize (*Zea mays* L.) and the effects of variable-rate nitrogen (N) application on crops. Images of a 27-ha maize field were captured using a UAV with a consumer-grade RGB camera flying at ~100 m above ground level at three maize growth stages. The collected sequential images were stitched and the Excess Green (ExG) colour feature was extracted to develop prediction models for maize yield and to examine the effect of the variable-rate N application. Various linear regression models between ExG and maize yield were developed for three sample area sizes (21, 106, and 1058 m$^2$). The model performance was evaluated using coefficient of determination ($R^2$), F-test and the mean absolute percentage error (MAPE) between estimated and actual yield. All linear regression models between ExG and yield were significant ($p \leq 0.05$). The MAPE ranged from 6.2 to 15.1% at the three sample sizes, although $R^2$ values were all <0.5. Prediction error was lower at the later growth stages, as the crop approached maturity, and at the largest sample level. The ExG image feature showed potential for evaluating the effect of variable-rate N application on crop growth. Overall, the low-cost UAV imaging system provided useful information for field management.

© 2019 IAgrE. Published by Elsevier Ltd. All rights reserved.

## 1. Introduction

Crop yield prediction is important for farmers to improve crop management both within the growing season and from one year to the next, especially for applications of crop insurance, harvest planning, grain storage requirements, cash flow budgeting, and for determining inputs like nutrients, pesticides, and water (Geipel, Link & Claupein, 2014). Crop yield may be estimated

---

using destructive sampling methods, which are labour intensive and time consuming (Lauer, 2002). In many cases, yield is estimated based on the expert knowledge of farmers and/or other professionals, or yield maps from previous years (Blackmore, 2000), methods which are subjective and not accurate. In addition, crop growth models have been used to predict yield based on historical data that might vary year by year (Corbeels, Chirat & Messad, 2016; Krishnan et al., 2016; Wang, Li, Lu, & Fang, 2013). With the development of remote sensing technology, various systems have been applied for larger-scale and non-destructive crop monitoring and measurement that can be used for yield estimation (Aasen, Honkavaara, Lucieer, & Zarco-Tejada, 2018; Lamb & Brown, 2001; MarketsandMarkets, 2013; Zhang & Kovacs, 2012; Zhang, Qin, Liu, & Ustin, 2003). However, some issues for crop yield estimation include low estimation accuracy and high cost of sensors and imaging systems.

Compared with satellite remote sensing systems, low-altitude remote sensing systems based on UAVs have been found appropriate for crop field scouting with the advantages of lower cost, user-friendly operation, flexibility, and very-high image resolution (less than 1 cm pixel$^{-1}$) (Colomina & Molina, 2014; Jannoura, Brinkmann, Uteau, Bruns & Joergensen, 2015; Vega, Ramírez, Saiz & Rosúa, 2015). UAV-based remote sensing systems usually include various imaging sensors to capture different types of structure and reflectance information of crops, including visible, hyper- or multi-spectral, or thermal cameras. Information collected from remote sensing systems can be used to calculate different image features (e.g., colour, spectral, temperature, and crop morphological features) for evaluation of agronomic crop traits and performance, including yield. Colour features derived from visible range of wavelengths (400—700 nm) have been used to recognise plant type or discriminate fruits from background (e.g., soil, weeds) (Jannoura et al., 2015; Woebbecke, Meyer, Vonbargen & Mortensen, 1995; Zheng, Zhu, Huang, Guo & Qin, 2017; Zhou, Damerow, Sun & Blanke, 2012). Spectral features based on combinations of visible and near-infrared (700—1000 nm) wavelengths, including vegetation indices (VIs) such as the normalised difference vegetation index (NDVI), have often been used to monitor crop growth or predict crop yield (Guo et al., 2017; Nebiker, Lack, Abächerli & Läderach, 2016; Panda, Panigrahi & Ames, 2010; Xue & Su, 2017). Data from infrared wavelengths (7500—13,000 nm) can estimate surface temperature and may be used to provide an early response to crop water stress prior to appearance of visual symptoms (Bulanon, Burks & Alchanatis, 2008; Khanal, Fulton & Shearer, 2017; Mangus, Sharda & Zhang, 2016; Sepulcre-Cantó et al., 2006). In recent years, crop height quantified from a crop surface model (CSM) obtained using a UAV imaging system has been used to predict yield (Feng, Zhang, Sudduth, Vories & Zhou, 2019; Huang et al., 2016; Malambo et al., 2018; Yin, Jaja, McClure & Hayes, 2011). Integration of multiple sensors can improve the sensing accuracy and reliability (Bendig et al., 2015; Maimaitijiang et al., 2017; Pantazi, Moshou, Alexandridis, Whetton & Mouazen, 2016; Turner, Lucieer, Malenovský, King & Robinson, 2014), but increased payload weight, cost (i.e., computing and hardware) and complexity in system architecture and data analysis (Zhang & Kovacs, 2012) are obstacles that must be overcome.

Compared with spectral, temperature, and crop morphological features, visible colour as a compositae of red-green-blue (RGB) values, may represent the most intuitive way to monitor the status of crops. A simple-to-use and low-cost tool used to assess crop health and make N application recommendations since the 1990s was the Leaf Colour Chart (LCC) with four or six panels of gradient green colour (Balasubramanian, Morales, Cruz & Abdulrachman, 1998; Friedman, Hunt & Mutters, 2016; Shukla et al., 2004). This widely-used measurement can be inexpensively obtained using a consumer grade RGB camera. The crop canopy can exhibit a different colour due to different growing conditions and variation in chlorophyll content (Hörtensteiner & Matile, 2004, pp. 189—202). For instance, crop canopy colour has been used to diagnose nitrogen (N) deficiency since N-deficient crops are lighter green in colour than healthy crops (Stevens, Motavalli, Scharf, Nathan & Dunn, 2002). Crop colour features have been used to monitor crop biomass and growth status based on single or combined indices from different colour models, including RGB, HSI (hue, saturation, intensity) and Lab (lightness, green—red and blue—yellow). Some examples of features include simple ratios [G/R (G-B)/(G + B) and (G-R)/(G + R)], combinations [2G-R-B (2G-R-B)/(2G + R + B)], normalised RGB [R/(R + B + G), G/(R + B + G) and B/(R + B + G)], hue in HSI, and lightness in Lab (Ahmad & Reid, 1996; Du & Noguchi, 2017; García-Mateos, Hernández-Hernández, Escarabajal-Henarejos, Jaén-Terrones & Molina-Martínez, 2015; Gracia-Romero et al., 2017; Jannoura et al., 2015; Lee & Lee, 2013; Meyer & Neto, 2008; Xue et al., 2017; Yang, Wang, Zhao, Zhang, & Feng, 2015). Gracia-Romero et al. (2017) found that RGB-based indices were the best option for evaluating maize performance and grain yield under different phosphorus nutrient conditions. Additional evaluation of the use of RGB colour features for yield estimation of various crop under a wide range of environmental conditions is worthy of additional study.

Mathematical models for crop yield estimation can be divided into two main methods, i.e. classification and regression. The classification method can use statistical or machine-learning methods to classify crop yields into several classes based on image features. Panda et al. (2010) classified maize yield to low, medium and high classes by using a self-organizing map and Supervised Kohonen Networks (SKNs) for predicting maize yield in a 65-ha field. Pantazi et al. (2016) classified wheat yield to low, medium and high classes by using counter-propagation artificial neural networks, XY-fused networks and SKNs for predicting wheat yield in a 22-ha field. Prediction models based on machine learning are powerful in dealing with complicated datasets with multiple inputs and outputs (Chlingaryan, Sukkarieh & Whelan, 2018); however, using complicated statistical algorithms increases the potential of overfitting. One the other hand, simple regression models, including linear regression have the features of simplicity, expandability and acceptable performance, which is why linear regression has often been used in research to develop models for crop yield prediction. For example, Yin et al. (2011) compared linear regression models with quadratic, square root, logarithmic and exponential models in assessing the relationship of maize yield to plant height, and found that the linear regression model gave the best results. Geipel et al. (2014) used three different linear regression models for predicting maize yield based on plant

height and crop canopy coverage. The models exhibited $R^2$ up to 0.74 and root mean squared error (RMSE) of prediction from 0.67 to 1.28 t ha$^{-1}$ (8.8%–16.9%). Du and Noguchi (2017) developed stepwise multiple linear regression models for predicting wheat yield based on RGB colour indices, including the excess green vegetation index (ExG = 2G-R-B). The published research indicates that there is high potential to use a UAV imaging system as a tool to estimate crop yield.

The UAV market is growing at a fast pace and in 2017 it was expected to triple from the annual value of $4 billion to $14 billion by 2027 (Canetta, Mattei & Guanziroli, 2017). Many commercial services have begun providing services to farmers and researchers for data collection and analysis. However, commercial algorithms are often secret and proprietary, and may have been developed for specific conditions. Therefore, more public studies are needed to bridge the gap between the technologies and their applications. The data provided by companies may be based on limited experiments with specific crops and field conditions. More research to confirm the potential of such technologies in different environmental conditions is needed. The primary objective of this investigation was to predict maize yield using a colour feature extracted from UAV-based consumer-grade RGB images (400–700 nm) of a maize field. A secondary objective was to evaluate the colour feature for distinguishing crop response to variable-rate N application.

## 2. Materials and methods

### 2.1. Field experiment

The experiment was performed on a portion of a 36-ha experimental field located near Centralia, Missouri, USA (39°13′46.3″N, 92°07′11.3″W). Soils on the field using the USDA classification (USDA NRCS, 2000) were predominately Adco silt loam (fine, smectic, mesic VerticAlbaqualfs) with 0–1% slopes at the summit position, Mexico silty clay loam (fine, smectic, mesic VerticEpiaqualfs) with 1–3% slopes at the back slope position, and Mexico silt loam or silty clay loam with <1% slope at the foot slope position. These soils are typical claypan soils with abrupt clay-rich layers at shallow depths, and equivalent to Luvisols using the FAO classification system (FAO/ISRIC/ISSS, 1998). The portion of the field included in this assessment was ~450 × 600 m$^2$ (27 ha).

Maize (Golden Harvest G14R38-3000 GT) was planted using a 6-row planter on April 15, 2016 at a population of 79K seeds ha$^{-1}$ on a 76-cm row spacing. Fertiliser N was broadcast applied at planting at a fixed rate of 54 kg N ha$^{-1}$, with a small portion of the field (<6%) receiving an additional 222 kg N ha$^{-1}$ to provide an N-rich reference strip used for determining in-season variable-rate N applications. On June 3, at ~ V6 growth stage (Hanway, 1986), Fertiliser N was again broadcast applied at a fixed rate of 54 kg N ha$^{-1}$. On June 22, at ~ V10 growth stage, a variable-rate N application was side-dressed (i.e. placed between the crop rows) on the soil surface. After broadcasting Fertiliser on the whole field, the maize plant still grew differently under different conditions, a function of variable soil across the landscape impacting N mineralization, transport, and loss processes (Kitchen, Goulding & Shanahan,

2008). Therefore, side-dress application was used to help those unhealthy plants grow healthy based on a ground-based canopy reflectance sensing. The side-dress application rate was determined using ground-based canopy reflectance sensors and a decision algorithm as previously documented (Kitchen et al., 2010; Sudduth, Drummond & Kitchen, 2015). The working width of the Fertiliser applicator was six rows. The Fertiliser application rate and the corresponding GPS data were recorded at 1Hz, giving 14,665 N application data points. Eight discrete N rates ranging from 0 to 115 kg N ha$^{-1}$ on an increment of 19 kg N ha$^{-1}$ were used in the variable-rate application. By merging those N rates that were applied on only small areas, the field was classified into four levels of N application. As shown in Fig. 1b, N rate Level 1 referred to 108 kg ha$^{-1}$, accounting for 39.2% of field area; Level 2 referred to 127,146 and 166 kg ha$^{-1}$, accounting for 11.0% of field area; Level 3 referred to 185, 204 and 223 kg ha$^{-1}$, accounting for 10.5% of field area; and Level 4 referred to 242 kg ha$^{-1}$, accounting for 33.3% of field area. The spatial variation in overall N application (i.e., combining all three applications) is illustrated in Fig. 1a.

Grain was harvested on September 30, 2016 with a Gleaner R42 combine harvester (AGCO Corporation, Duluth, GA, USA), equipped with an Ag Leader yield monitor (Ag Leader Technology, Ames, IA, USA) that recorded the geo-referenced maize yield and grain moisture at a 1 Hz frequency. The harvest width was six rows, following the same 6-row swaths used in planting and variable-rate N application. After harvesting, raw yield data ($n = 14,705$) were processed with Yield Editor software (Sudduth, Drummond & Myers, 2012) to remove data artefacts.

### 2.2. RGB image collection

Images of the maize field were collected using a UAV (Phantom 3, DJI, Shenzhen, China) equipped with an on-board digital RGB camera (resolution: 4000 × 3000 pixels) at sample rate of 0.5 frame per second. RGB images were collected using the UAV at three reproductive growth stages: kernel development (~R2; July 12), grain filling (~R3; July 18), and physiological maturity (~R6; August 19). The UAV system flew at a height of 100 m above ground level. A UAV flight control app (DroneDeploy, San Francisco, CA, USA) was used to plan the flights, including waypoints, flight height, and camera snapshot rate, to acquire images with 75% overlap. The sequential images were geo-referenced using the GPS of the UAV. Images were uploaded to a commercial cloud server (DroneDeploy) to generate "stitched" panoramic images for further processing.

### 2.3. Geo-registration

To estimate the maize yield and evaluate the effect of N application on crop growth, the geo-referenced yield data (map) and the N application data were registered with the imagery data collected on each of the three days. The only connection between imagery data and ground data was the geo-referencing information. Therefore, the GPS coordinates of the stitched images were first adjusted using Google Earth (Benker, Langford & Pavlis, 2011; Mohammed, Ghazi & Mustafa, 2013). Three fixed objects in the maize field,
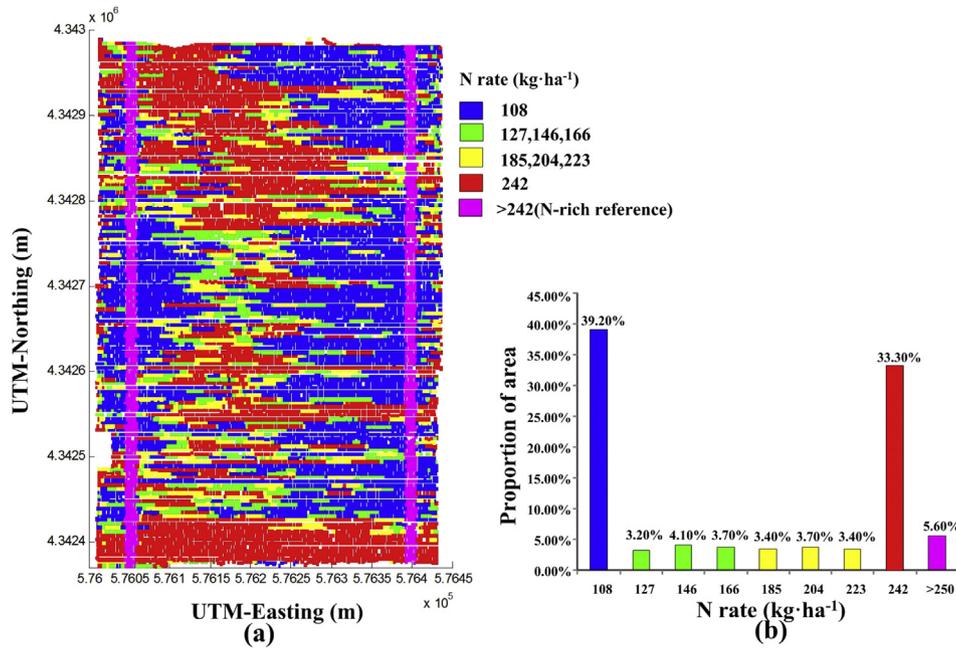
**Fig. 1 − Illustration of total N application rate. (a) Application map, where intermediate N rates are grouped together for visualization. (b) N rate application levels and the corresponding percentages of field area.**

including one building, one tree and one fence gate, that were visible in all the stitched images and the Google Earth image were selected as ground control points (GCPs), and their GPS coordinates were extracted from Google Earth. One GCP was set as the origin point for GPS data $(x_{g0}, y_{g0})$ and the corresponding pixels in the image $(x_{p0}, y_{p0})$, and another two GCPs were used to calculate the scale factor $(k_x, k_y)$ using GPS data $(x_{g1}, y_{g1})$ and $(x_{g2}, y_{g2})$ and two corresponding image pixels $(x_{p1}, y_{p1})$ and $(x_{p2}, y_{p2})$. The conversion formulae used were are as follows:

$$\begin{cases} x_{y\_pi} = \left(x_{y\_gi} - x_{g0}\right) \times k_x + x_{p0} \\ y_{y\_pi} = \left(y_{y\_gi} - y_{g0}\right) \times k_y + y_{p0} \\ x_{n\_pi} = \left(x_{n\_gi} - x_{g0}\right) \times k_x + x_{p0} \\ y_{n\_pi} = \left(y_{n\_gi} - y_{g0}\right) \times k_y + y_{p0} \end{cases}, \begin{cases} k_x = \left|x_{p1} - x_{p2}\right| / \left|x_{g1} - x_{g2}\right| \\ k_y = \left|y_{p1} - y_{p2}\right| / \left|y_{g1} - y_{g2}\right| \end{cases}$$

(1)

where, $(x_{y\_gi}, y_{y\_gi})$ and $(x_{y\_pi}, y_{y\_pi})$ are a yield GPS coordinate and its converted image coordinate of the ith yield data, and $(x_{n\_gi}, y_{n\_gi})$ and $(x_{n\_pi}, y_{n\_pi})$ are a N application GPS coordinate and its converted image coordinate of the ith N application data. The adjusted geo-referenced stitched images were matched separately to the geo-referenced yield and N application data. Each yield data point represented an approximate field area of 4.6 m × 4.6 m based on the harvest width (six rows), the travel speed of the combine harvester, and the sampling frequency of the yield monitor. A region-of-interest (92 × 92 pixels) in the images corresponding to each yield point was defined as a sample cell $\{(x_{y\_gi}, y_{y\_gi}) , i = 1, 2, 3 \ldots n_y\}$ and was used in further analysis. As shown in Fig. 2, the blue points in the left image were yield points distributed on the adjusted images, and the red squares are the sample cells corresponding to each yield point. The same procedure was

also used to define the sample cells $\{ (x_{n\_gi}, y_{n\_gi}) , i = 1, 2, 3 \ldots, n_n\}$ for the N application data.

### 2.4. Extraction of image feature

Colour features extracted from the RGB images of the three growth stages were used to evaluate the potential of image data for the estimation of maize yield and evaluation of variable-rate N application. Among different existing colour models, the RGB colour model is the most commonly used in various applications and can be converted to other colour spaces (e.g. HSV, HSI or Lab) through linear or nonlinear conversion (Łuszczkiewicz-Piątek, 2014). Different combinations of the three components in the RGB model have been used to enhance the contrast of crop to background pixels for removing backgrounds, including ExG, normalised RGB and differences [(R−B) and (G−R)] (Jannoura et al., 2015; Zheng et al., 2017; Zhou et al., 2012). Among the colour features, ExG has been widely used to segment plants from background, monitor crop N stress and estimate yield (Du & Noguchi, 2017; Geipel et al., 2014; Woebbecke et al., 1995; Zheng et al., 2017). Given these previous findings, ExG was selected as the colour feature for developing yield estimation models. The mean of ExG in each sample cell as defined in Fig. 2 was calculated as the value corresponding to the yield data point in that cell, and the resulting data pairs were used as data sets for modelling.

### 2.5. Modelling and evaluation indexes

Yield estimation models were developed using the developed data sets (pairs) of the three growth stages separately. Various linear and nonlinear regression models including parametric,
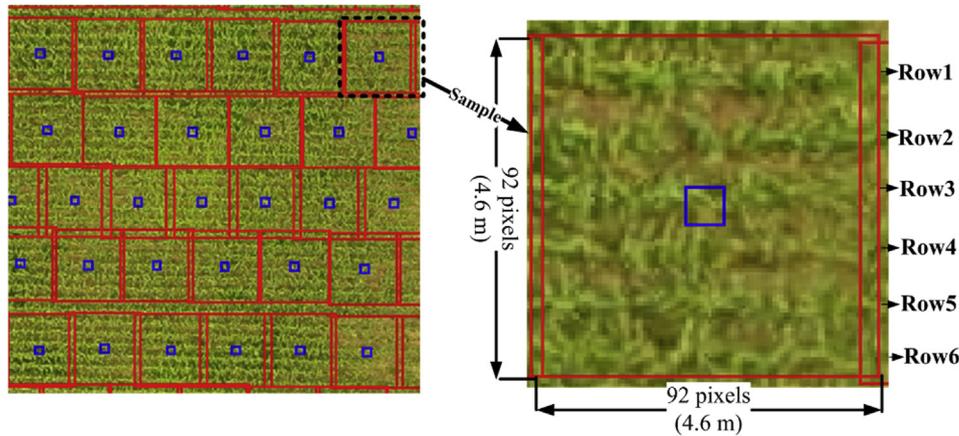
Fig. 2 – Images show an example of how a stitched image was processed into 92 × 92 pixel sample cells for yield data, with an area of ~ 4.6 × 4.6 m per cell, which was equivalent to the 6-row combine width. Right photo shows one sample cell including six rows.

least-square, polynomial, exponential and power fittings in the Curve Fitting Toolbox of Matlab were tested to estimate crop yield with the colour feature ExG. After comparing the preliminary results (not reported), linear regression models showed the least errors. Therefore, a linear regression was used to estimate crop yield using the colour feature ExG, with 80% of the data at each stage randomly chosen as the training data for developing the models and the remaining 20% used for evaluating the model accuracy. The slopes and intercepts of the models were calculated by the Curve Fitting Toolbox based on the least squares method (Martin, 2012). The operation was repeated by choosing sequential partitions of the data sets with a random initial value (Kamilaris & Prenafeta-Boldú, 2018). The standardised residual $e_i^*$ (Eq. (2); Hayter, 2012) of the model was analysed to characterise the distribution of the outliers in the field.

$$e_i^* \cong \frac{e_i}{\widehat{\sigma}} = \frac{y_i - \widehat{y}_i}{\sqrt{\frac{\sum_{i=1}^{n}(y_i - \widehat{y}_i)^2}{n-2}}}, \sum_{i=1}^{n} e_i = 0 \qquad (2)$$

where, $y_i$ is the observed values, $\widehat{y}_i$ is the corresponding fitted values, and $n$ is the number of points. The model performance was evaluated using the coefficient of determination ($R^2$), $p$-value, and mean absolute percentage error (MAPE) between estimated and measured data. The $R^2$ was used to measure model adequacy, the $p$-value was used to analyse the significance of the model by $F$-test based on analysis of variance (ANOVA) (Hayter, 2012), and MAPE was used to evaluate model accuracy. Whether the model accuracy (MAPE) was affected by crop growth stage and area size was evaluated by ANOVA (Hayter, 2012). The MAPE was examined at three area sizes: 1) one sample cell per area (21 m²); 2) five sample cells per area (106 m²); and 3) 50 sample cells per area (1058 m²). In the testing data (20% of whole data, 12,500 × 0.2 = 2500), there were 2500 samples in 21 m² (one sample cell per area), 500 samples in 106 m² (five sample cells per area), and 50 samples in 1058 m² (50 sample cells per area) as listed in Table 1. The equations used to calculate the MAPEs are given in Table 1.

### 2.6.    Evaluation of variable-rate fertilization

The goal of variable-rate N application is to optimise the amount of fertiliser applied to match crop need at each point in the field. However, crop growth and yield potential at any given crop growth stage could vary spatially due to soil and field topography, resulting in unique responses to N application in different areas of the field. To evaluate crop response to the variable-rate N application, the means and standard deviations of ExG within four levels (Fig. 1) of applied N were analysed by ANOVA at each of the three crop growth stages to examine spatial and temporal crop variation.

## 3.    Results and discussion

### 3.1.    Cleaned yield data

Raw yield data were cleaned using the Yield Editor 2.0 program to eliminate artefacts of the data collection procedure such as errors where the combine harvester entered and exited from the crop. About 15% of the raw data were removed using the filters and procedures described in Sudduth et al. (2012). The distribution of the raw yield data over the field is shown in Fig. 3a, and the histograms of both raw and pre-processed data are provided in Fig. 3b. The histogram of Fig. 3b shows that data removal largely came from the tails of the distribution and cleaned yield data was approximately normal in distribution. Removed data (pink in Fig. 3a) were mainly on the field edges (in the case of the south and east edges, adjacent tree lines created resource competition between crop and trees), and along a major water flow channel running north and south near the centre of the field. While the crop was planted continuously through the flow channel, persistent wet conditions during germination and emergence resulted in a poor crop stand in this part of the field and the area was dominated by weeds by mid-summer. Data removal was justified because crop growth and/or stand were compromised in these areas.

**Table 1 – Equations and information about MAPE.**

| Level | Sample area (m$^2$) | Number of samples | Measured yield in each sample[a] | MAPE[b] |
|---|---|---|---|---|
| 1 | 21 | $n_1 = 2500$ | $y_{1\_j} = y_i$<br>$i = j = 1, 2, 3 ... n_1$ | $MAPE_1 = \frac{1}{n_1}\sum_{j=1}^{n_1}\left(\frac{\left|y_{1\_j} - \hat{y}_{1\_j}\right|}{y_{1\_j}} \times 100\%\right)$ |
| 2 | 106 | $n_2 = 500$ | $y_{2\_j} = \sum_{i}^{i+4} y_i$<br>$j = 1, 2, 3 ... n_2$<br>$i = 1, 5, 10 ... n_1$ | $MAPE_2 = \frac{1}{n_2}\sum_{j=1}^{n_2}\left(\frac{\left|y_{2\_j} - \hat{y}_{2\_j}\right|}{y_{2\_j}} \times 100\%\right)$ |
| 3 | 1058 | $n_3 = 50$ | $y_{3\_j} = \sum_{i}^{i+49} y_i$<br>$j = 1, 2, 3 ... n_3$<br>$i = 1, 50, 100 ... n_1$ | $MAPE_3 = \frac{1}{n_3}\sum_{j=1}^{n_3}\left(\frac{\left|y_{3\_j} - \hat{y}_{3\_j}\right|}{y_{3\_j}} \times 100\%\right)$ |

[a] There was no overlap between the samples.

[b] $\hat{y}_{1\_j}$, $\hat{y}_{2\_j}$ and $\hat{y}_{3\_j}$ are the estimated yield in each sample size, and estimated yield value was set to zero if less than zero because the yield data were all non-negative values.
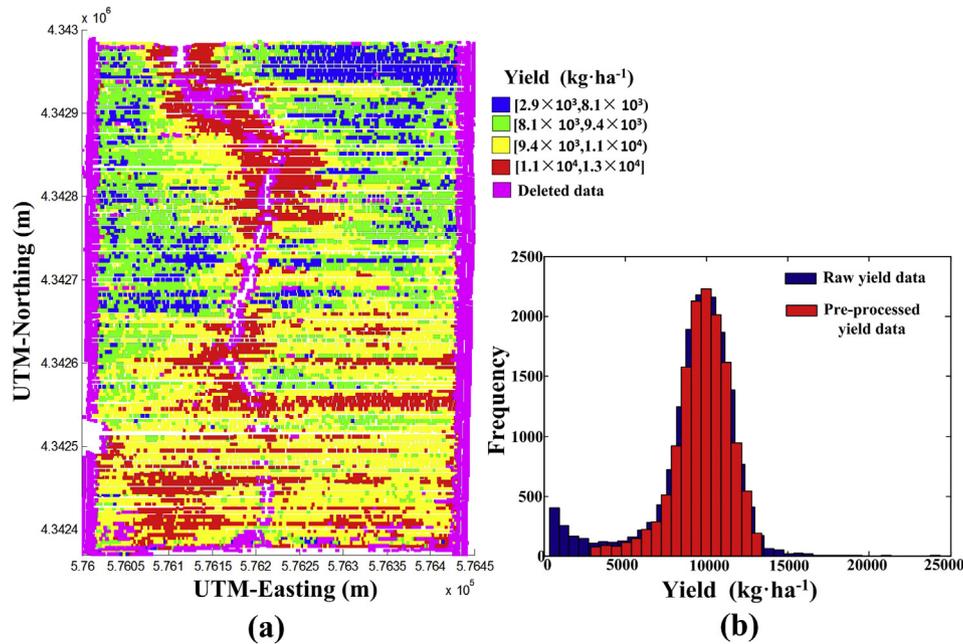


**Fig. 3 – Illustration of yield data in the field. (a) Yield map. (b) Histograms of raw and cleaned yield data.**

### 3.2. Image data processing

The stitched RGB images and ExG images for the three growth stages (R2, R3, and R6) are shown in Fig. 4. As the crop matured, spatial differences in the RGB images became more apparent, with a pattern similar to the pattern of N application (Fig. 1). There was an obvious difference between the ExG image collected at growth stage R6 (Fig. 4f) and the ExG images at R2 and R3 (Fig. 4d, e) because the crop colour transformed from green to yellow as the crop developed towards physiological maturity (R6). The test area of the field was approximately 450 m × 600 m for a corresponding image size of 9000 × 12,000 pixels, resulting in a resolution of ~400 pixels m$^{-2}$. The position of each yield data point on the images was calculated according to Eq. (1), and yield points are shown in a portion of the field as blue dots (Fig. 2, left). The sample area

corresponding to each yield point was approximately 4.6 m × 4.6 m, therefore, sample cells on the image were defined with size 92 × 92 pixels around each yield data point as shown by the red squares in Fig. 2. Some cells overlapped due to GPS coordinate errors, variation in travel speed, or changes in harvester heading. However, only a small portion of each cell overlapped and therefore this overlap was ignored in the analysis. The average ExG value was calculated for each cell and matched with the corresponding yield, resulting in a total of 12,500 cells of merged data.

### 3.3. Prediction models for yield

Yield prediction models were developed using the UAV-based ExG colour feature extracted at the three maize growth stages (R2, R3, and R6) to test yield estimation potential in
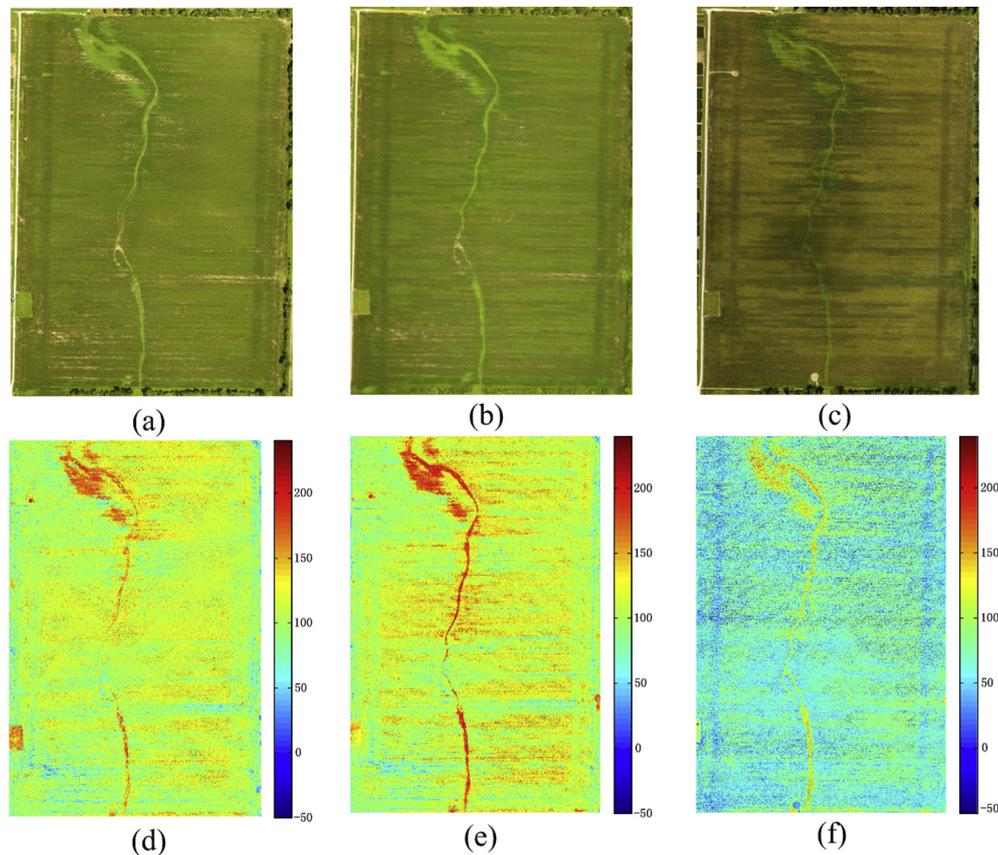
**Fig. 4 – Stitched panoramic RGB and ExG images. (a)–(c) are the stitched panoramic images acquired at maize growth stages of R2, R3, and R6 (taken on July 12, July 18 and August 19, 2016, respectively). (d)–(f) are pseudo-colour ExG images converted from three stitched RGB images (a)–(c), respectively.**

reproductive growth stages. Regression results showing yield as a function of ExG at the three stages are shown in Fig. 5a–c. Results show that Yield was correlated to ExG at all growth stages ($p < 0.05$), but the correlation was stronger in later stages, as seen by the higher $R^2$ and regression slope at the R6 stage. It can be seen that the $R^2$ for all models were less than 0.5, which might be due to the limitations of the low-cost sensor (camera). According to the study conducted by Jang, Sudduth, Hong, Kitchen & Palm (2006) in the same field as this study, the spectral bands in the near infrared range (780–850 nm) had higher correlation with maize yield than visible bands in early growth stages, but $r$ was still in a low range (around 0.2–0.8). However, the combination of short near infrared (849 nm) and red (716 nm) obtained a stronger correlation ($r = ~0.85$). By reviewing the published studies, we also found that the $R^2$ for regression models or $r$ for correlations between predicated and measured yield were always not high regardless of data collection platforms and models. For example in the study reported by Panda et al. (2010), the correlation coefficients between measured yield and estimated yield using different models ranged from 0.20 to 0.78 for different years, although the reported estimation accuracy was as high as 95%. Geipel et al. (2014) reported that the $R^2$s for maize yield using ExG derived from UAV-based imagery could be as low as 0.48, even with high-resolution images and complicated strategies. A more recent study estimating maize

yield (Gao, Anderson, Daughtry & Jonson, 2018) showed a range of $r = 0.46$–0.63 with different high-resolution satellite imagery.

To explore the errors that may cause low $R^2$ in regression models based on the ExG colour feature, the standardised residuals of the models for the three stages were plotted in Fig. 5d–f, which show approximately 15% of the data exhibited an absolute standardised residual >3 (as marked in red in Fig. 5). These points were considered to be outliers (Hayter, 2012). The residuals for these points were negative, indicating that estimated yield was considerably greater than measured yield. To identify the potential reasons for such outliers, these data points were overlaid on the corresponding RGB images (Fig. 6), but no consistent spatial pattern was observed. These outliers might be the result of random system error, perhaps due to GPS or yield monitoring system errors, or non-uniformity of the image cells.

For each growth stage, MAPE was calculated based on three levels of sample area size, 21 m$^2$, 106 m$^2$ and 1058 m$^2$. The average values of MAPE with $\pm 1.96 \times$ SE (Standard Error at 95% confidence interval) were used to analyse prediction error (Hayter, 2012). Results from ANOVA comparing the difference in mean yield prediction errors for the three crop growth stages are shown in Fig. 7. Analyses compare means of growth stage within each sample area size (7a), as well as the sample area size within each growth stage (7b). Prediction error was
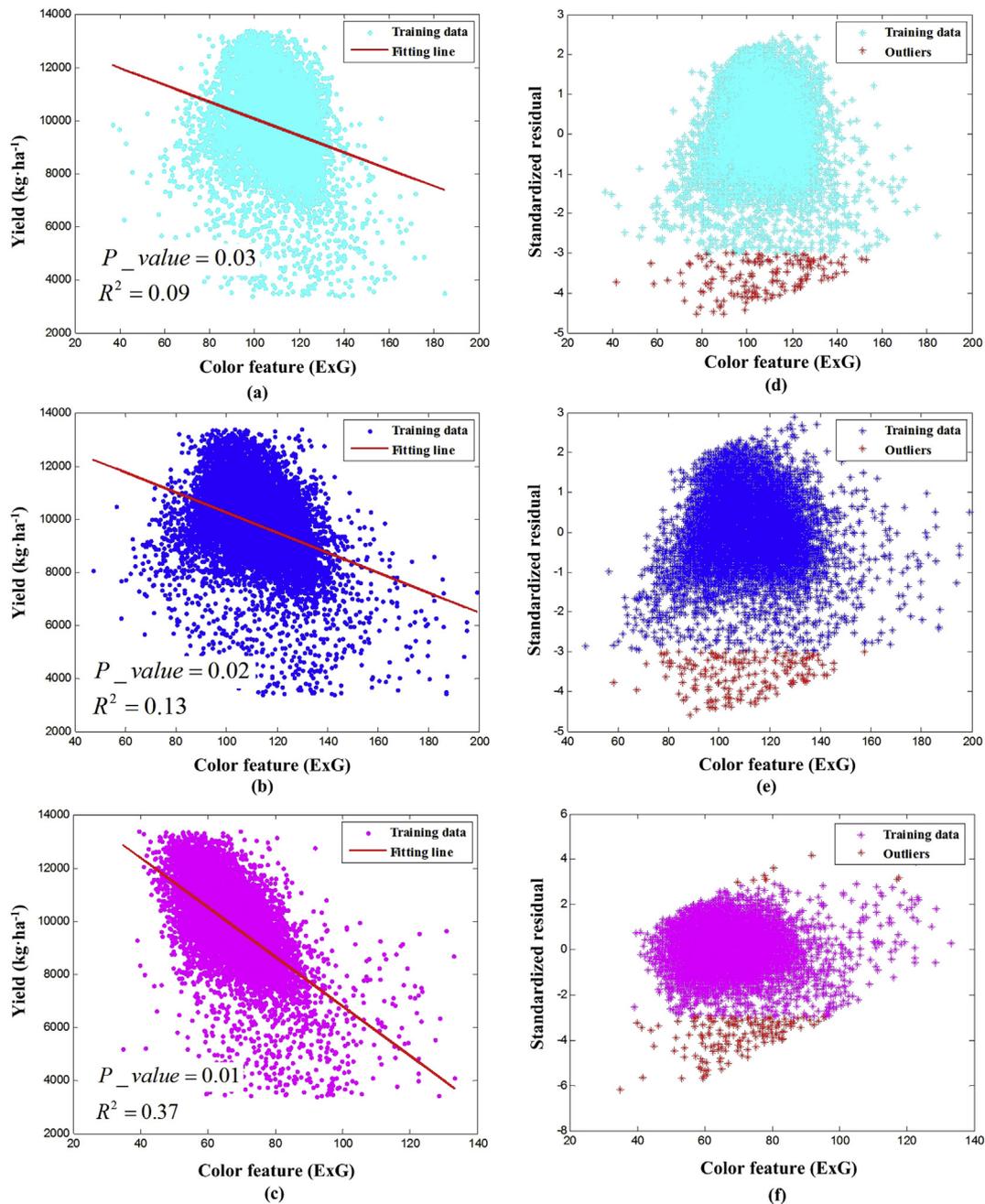
**Fig. 5 – Regression analysis between the colour feature (ExG) and yield using data sets obtained at three growth stages. Sub-figures (a)–(c) are scatter plots of regression fits for training data in growth stages of R2, R3 and R6, respectively. The corresponding regression models are $y = -38.7x + 1.4 \times 10^4$, $y = -44.2x + 1.5 \times 10^4$, and $y = -93.2x + 1.6 \times 10^4$. Sub-figures (d)–(f) are standardised residual plots associated with the models in (a)–(c), respectively. (For interpretation of the references to colour in this figure legend, the reader is referred to the Web version of this article.)**

affected by the growth stage for sample areas of 21 and 105 m², with significantly lower error as growth stage progressed. The lack of difference between growth stages at the largest sample area could be explained by the equalizing of crop variation with the larger sample area. When sample size was examined within each growth stage (7b), prediction error decreased with increasing sample size for all growth stages. However, it is important to note that the largest sample area used here would generally be considered too large for site-specific information collection and subsequent precision management

(Heege, 2015). Overall, the yield estimation errors of 6.2–15.1% were comparable with other remote sensing studies; errors ranged from 8.8 to 16.9% in Geipel et al. (2014) and were ~20% in Panda et al. (2010).

### 3.4. Evaluation of variable-rate fertilization

Crop differences represented by the ExG colour feature were related to spatial variations in N application that occurred earlier in the season. The results of an ANOVA *F*-test
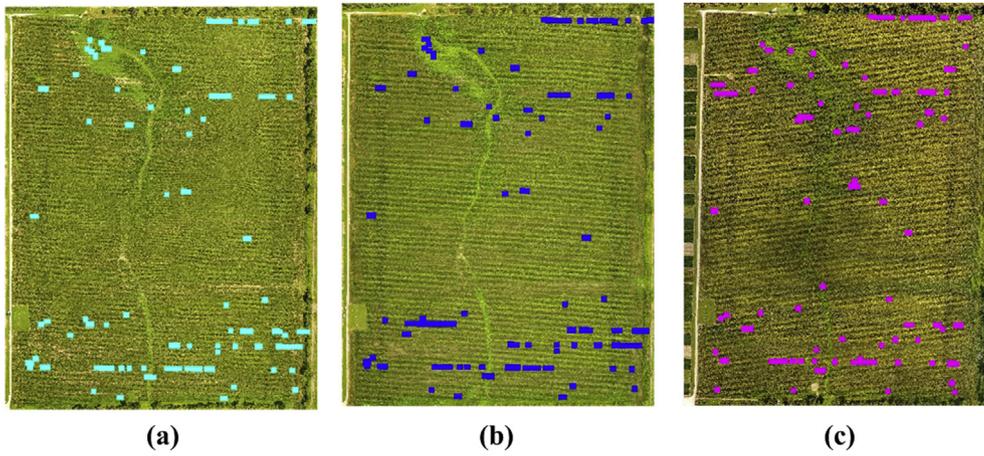
**Fig. 6 − Distribution of outliers on the field at the three growth stages of R2 (a), R3 (b), and R6(c).**
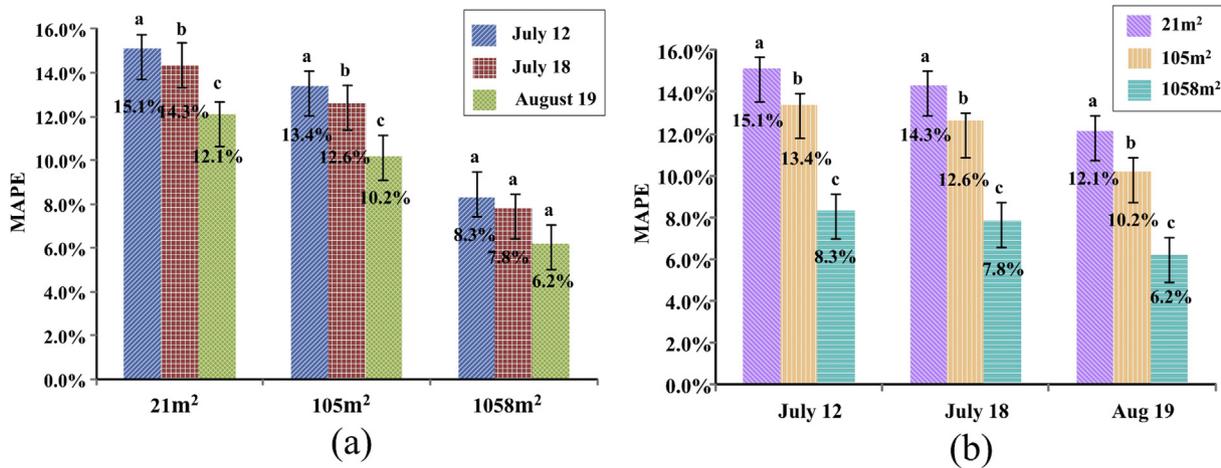


**Fig. 7 − ANOVA analysis of MAPE at three area levels using data acquired at three growth stages of R2, R3 and R6. (a) Comparison of mean MAPE (with standard deviations) at different growth stages within each sample area with $\pm 1.96 \times$ SE (Standard Error) error bar. (b) Comparison of mean MAPE (with standard deviations) at different levels of sample area within each growth stage with $\pm 1.96 \times$ SE error bar. Mean MAPE bars with different lower case letters are significantly different within each group.**
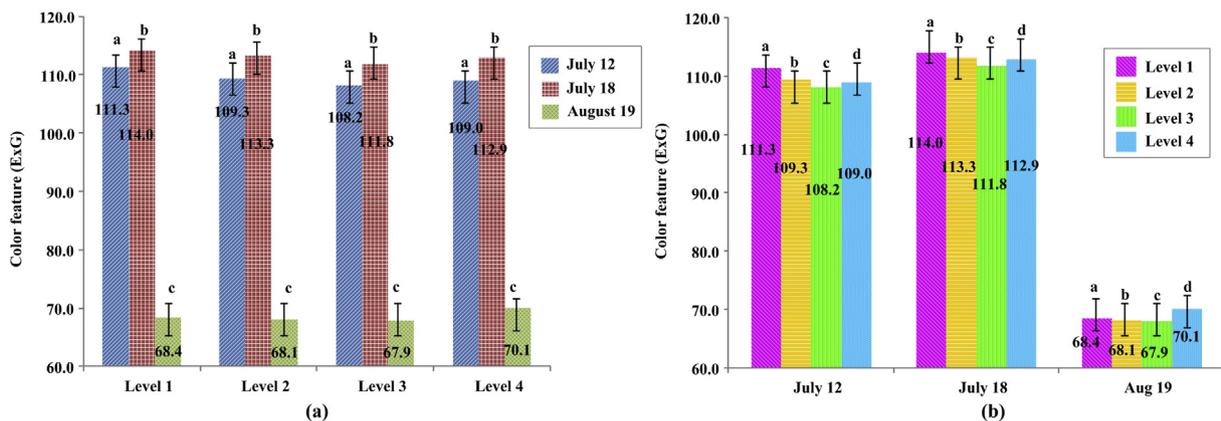


**Fig. 8 − ANOVA analysis of crop growth at four N rate levels using data acquired at R2, R3 and R6. (a) Comparison of mean ExG (with standard deviations) at different crop growth stages within different levels of N application with $\pm 1.96 \times$ SE (Standard Error) error bars. (b) Comparison of mean ExG (with standard deviations) at different N application rates within three growth stages with $\pm 1.96 \times$ SE error bars. The different lower case letters indicate significant differences in mean ExG within each group.**
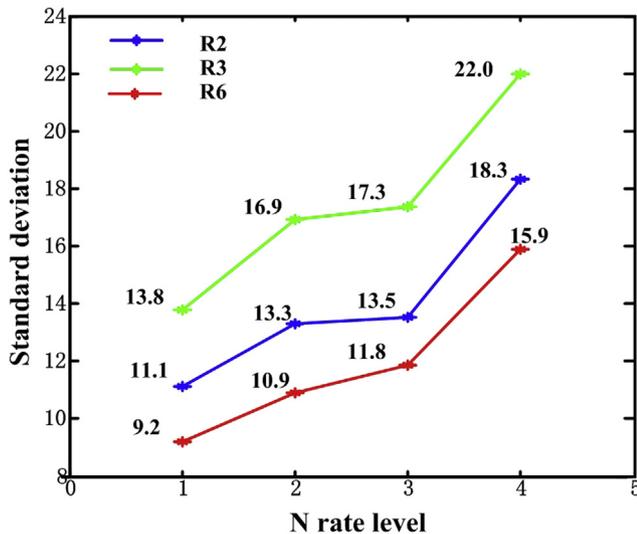
**Fig. 9 – Standard deviation of the ExG colour parameter for four N rate levels at each of three growth stages. (For interpretation of the references to colour in this figure legend, the reader is referred to the Web version of this article.)**

examining colour feature differences as a function of crop growth stages and N levels are shown in Fig. 8. The ExG value within each N level was significantly different by growth stage (Fig. 8a). Mean ExG values increased from growth stage R2 to R3, but decreased dramatically between R3 and R6 because the crop colour transformed from green to yellow with physiological maturity. The effects of variable-rate fertilization at different growth stages are shown in Fig. 8b. In the early growth stages, ExG was different by N level because N fertiliser was not fully absorbed by the crop. For the R6 growth stage the relatively small ExG differences between N levels suggest the crop condition relative to N health was similar, meaning that the goal of variable-rate fertilization to provide sufficient N in all parts of the field was at least somewhat successful.

In addition, Fig. 9 shows the standard deviation of ExG under different fertilization levels. Overall, the standard deviation in ExG increased from R2 to R3 (fertiliser application was prior to R2), and decreased from R3 to R6 (closer to physiological maturity). Regions with the lowest N application (Level 1, Fig. 9), due to exhibiting less N need at the time of side-dress fertilization, had the lowest ExG standard deviations, suggesting a more homogenous and steady growth of the crop. In contrast, regions with the highest N application (Level 4), due to exhibiting more N need at the time of side-dressing, had the highest ExG standard deviation. This suggests that non-N fertility factors causing differential crop development may have been more important in the Level 4 parts of the field.

## 4.     Conclusion

In this study, maize yield was predicted using remote colour imagery captured by a UAV imaging system. Multi-temporal images of a maize field were collected by the UAV system and the ExG colour parameter was calculated based on the RGB colour model to monitor the continuous spatial variation of the crop at three important growth stages, i.e. R2, R3 and R6. Linear regression models predicted maize yield using 80% of the raw data for training and 20% for testing. The accuracy of the prediction models was evaluated using MAPE based on the test data in three levels of sample area (21 m$^2$, 106 m$^2$, and 1058 m$^2$). Models estimating yield from ExG were all statistically significant at the 5% level. Specific conclusions were:

- A low-cost UAV RGB imaging system was able to estimate maize yield with mean absolute percentage error (MAPE) ranging from 6.2 to 15.1%, indicating a potential to be used in practise.
- The error of yield estimation was lower when using images closer to maturity.
- The UAV RGB images might be used to evaluate the effect of variable-rate N application.

In summary, this study demonstrated that a UAV imaging system can be a good tool for collecting site-specific field and crop information in precision agriculture. The crop colour information (ExG) shows promise in predicting within-field spatial variations in crop yield. The predicted maize yield data can be used as a feedback for harvesting operation decisions in the current year and fertilization decisions in the next year. Further studies are needed investigate the ability of remotely-sensed data to more accurately estimate within-field spatial variations in crop growth and yield. Better designed experiments will be needed to calibrate the imagery data to evaluate the effect variable-rate N application on plant growth.

## Acknowledgements

R E F E R E N C E S

Aasen, H., Honkavaara, E., Lucieer, A., & Zarco-Tejada, P. (2018). Quantitative remote sensing at ultra-high resolution with UAV spectroscopy: A review of sensor technology, measurement procedures, and data correction workflows. *Remote Sensing, 10*(7), 1091. https://doi.org/10.3390/rs10071091.

Ahmad, I. S., & Reid, J. F. (1996). Evaluation of colour representations for maize images. *Journal of Agricultural Engineering Research, 63*(3), 185–195. https://doi.org/10.1006/jaer.1996.0020.

Balasubramanian, V., Morales, A. C., Cruz, R. T., & Abdulrachman, S. (1998). On-farm adaptation of knowledge-

intensive nitrogen management technologies for rice systems. *Nutrient Cycling in Agroecosystems, 53*(1), 59–69. https://doi.org/10.1023/A:1009744605920.

Bendig, J., Yu, K., Aasen, H., Bolten, A., Bennertz, S., Broscheit, J., et al. (2015). Combining UAV-based plant height from crop surface models, visible, and near infrared vegetation indices for biomass monitoring in barley. *International Journal of Applied Earth Observation and Geoinformation, 39*, 79–87. https://doi.org/10.1016/j.jag.2015.02.012.

Benker, S. C., Langford, R. P., & Pavlis, T. L. (2011). Positional accuracy of the Google Earth terrain model derived from stratigraphic unconformities in the Big Bend region, Texas, USA. *Geocarto International, 26*(4), 291–303.

Blackmore, S. (2000). The interpretation of trends from multiple yield maps. *Computers and Electronics in Agriculture, 26*, 37–51.

Bulanon, D. M., Burks, T. F., & Alchanatis, V. (2008). Study on temporal variation in citrus canopy using thermal imaging for citrus fruit detection. *Biosystems Engineering, 101*(2), 161–171. https://doi.org/10.1016/j.biosystemseng.2008.08.002.

Canetta, L., Mattei, G., & Guanziroli, A. (2017). Exploring commercial UAV market evolution from customer requirements elicitation to collaborative supply network management. In *2017 international conference on engineering, technology and innovation (ICE/ITMC) (pp. 1016-1022). Funchal, Portugal, 27–29 June 2017* (pp. 1016–1022).

Chlingaryan, A., Sukkarieh, S., & Whelan, B. (2018). Machine learning approaches for crop yield prediction and nitrogen status estimation in precision agriculture: A review. *Computers and Electronics in Agriculture, 151*, 61–69.

Colomina, I., & Molina, P. (2014). Unmanned aerial systems for photogrammetry and remote sensing: A review. *ISPRS Journal of Photogrammetry and Remote Sensing, 92*, 79–97. https://doi.org/10.1016/j.isprsjprs.2014.02.013.

Corbeels, M., Chirat, G., Messad, S., & Thierfelder, C. (2016). Performance and sensitivity of the DSSAT crop growth model in simulating maize yield under conservation agriculture. *European Journal of Agronomy, 76*, 41–53. https://doi.org/10.1016/j.eja.2016.02.001.

Du, M., & Noguchi, N. (2017). Monitoring of wheat growth status and mapping of wheat yield's within-field spatial variations using color images acquired from UAV-camera system. *Remote Sensing, 9*(3), 289. https://doi.org/10.3390/rs9030289.

FAO/ISRIC/ISSS. (1998). *World reference base for soil resources. World soil resources report, #84*. Rome: FAO.

Feng, A., Zhang, M., Sudduth, K. A., Vories, E. D., & Zhou, J. (2019). Cotton yield estimation from UAV-based plant height. *Transactions of the ASABE, 62*(2), 393–404.

Friedman, J. M., Hunt, E. R., & Mutters, R. G. (2016). Assessment of leaf color chart observations for estimating maize chlorophyll content by analysis of digital photographs. *Agronomy Journal, 108*(2), 822. https://doi.org/10.2134/agronj2015.0258.

Gao, F., Anderson, M., Daughtry, C., & Johnson, D. (2018). Assessing the variability of corn and soybean yields in central Iowa using high spatiotemporal resolution multi-satellite imagery. *Remote Sensing, 10*(9), 1489.

García-Mateos, G., Hernández-Hernández, J. L., Escarabajal-Henarejos, D., Jaén-Terrones, S., & Molina-Martínez, J. M. (2015). Study and comparison of color models for automatic image analysis in irrigation management applications. *Agricultural Water Management, 151*, 158–166. https://doi.org/10.1016/j.agwat.2014.08.010.

Geipel, J., Link, J., & Claupein, W. (2014). Combined spectral and spatial modeling of corn yield based on aerial images and crop surface models acquired with an unmanned aircraft system. *Remote Sensing, 6*(12), 10335–10355. https://doi.org/10.3390/rs61110335.

Gracia-Romero, A., Kefauver, S. C., Vergara-Díaz, O., Zaman-Allah, M. A., Prasanna, B. M., Cairns, J. E., et al. (2017).

Comparative performance of ground vs. Aerially assessed RGB and multispectral indices for early-growth evaluation of maize performance under phosphorus fertilization. *Frontiers in Plant Science, 8*. https://doi.org/10.3389/fpls.2017.02004.

Guo, C., Zhang, L., Zhou, X., Zhu, Y., Cao, W., Qiu, X., et al. (2017). Integrating remote sensing information with crop model to monitor wheat growth and yield based on simulation zone partitioning. *Precision Agriculture, 19*(1), 55–78. https://doi.org/10.1007/s11119-017-9498-5.

Hanway, J. J. (1986). *How a corn plant develops. Special Report No. 48*. Ames, IA: Iowa State University of Science and Technology. Cooperative Extension Service.

Hayter, A. J. (2012). *Probability and statistics for engineers and scientists* (4th ed.). Boston: Richard Stratton (Chapter 11, 12).

Heege, H. J. (2015). Site-specific fertilizing. In H. J. Heege (Ed.), *Precision in crop farming* (pp. 193–271). Dordrecht, The Netherlands: Springer.

Hörtensteiner, S., & Matile, P. (2004). *12 - how leaves turn yellow: Catabolism of chlorophyll A2 - noodén, Larry D* plant cell death processes (pp. 189–202). San Diego: Academic Press.

Huang, Y., Brand, H. J., Sui, R., Thomson, S. J., Furukawa, T., & Ebelhar, M. W. (2016). Cotton yield estimation using very high-resolution digital images acquired with a low-cost small unmanned aerial vehicle. *Transactions of the ASABE, 59*(6), 1563–1574. https://doi.org/10.13031/trans.59.11831.

Jang, G. S., Sudduth, K. A., Hong, S. Y., Kitchen, N. R., & Palm, H. L. (2006). Relating hyperspectral image bands and vegetation indices to corn and soybean yield. *Korean journal of remote sensing, 22*(3), 183–197.

Jannoura, R., Brinkmann, K., Uteau, D., Bruns, C., & Joergensen, R. G. (2015). Monitoring of crop biomass using true colour aerial photographs taken from a remote controlled hexacopter. *Biosystems Engineering, 129*, 341–351.

Kamilaris, A., & Prenafeta-Boldú, F. X. (2018). Deep learning in agriculture: A survey. *Computers and Electronics in Agriculture, 147*, 70–90. https://doi.org/10.1016/j.compag.2018.02.016.

Khanal, S., Fulton, J., & Shearer, S. (2017). An overview of current and potential applications of thermal remote sensing in precision agriculture. *Computers and Electronics in Agriculture, 139*, 22–32. https://doi.org/10.1016/j.compag.2017.05.001.

Kitchen, N. R., Goulding, K. W. T., & Shanahan, J. F. (2008). Proven practices and innovative technologies for on-farm crop nitrogen management. In J. L. Hatfield, & R. F. Follett (Eds.), *Nitrogen in the environment* (pp. 483–517). Amsterdam, Netherlands: Elsevier Science, 2008.

Kitchen, N. R., Sudduth, K. A., Drummond, S. T., Scharf, P. C., Palm, H. L., Roberts, D. F., et al. (2010). Ground-based canopy reflectance sensing for variable-rate nitrogen corn fertilization. *Agronomy Journal, 102*(1), 71. https://doi.org/10.2134/agronj2009.0114.

Krishnan, P., Sharma, R. K., Dass, A., Kukreja, A., Srivastav, R., Singhal, R. J., et al. (2016). Web-based crop model: Web InfoCrop – wheat to simulate the growth and yield of wheat. *Computers and Electronics in Agriculture, 127*, 324–335. https://doi.org/10.1016/j.compag.2016.06.008.

Lamb, D. W., & Brown, R. B. (2001). PA-Precision Agriculture: Remote-sensing and mapping of weeds in crops. *Journal of Agricultural Engineering Research, 78*(2), 117–125. https://doi.org/10.1006/jaer.2000.0630.

Lauer, J. (2002). Methods for Calculating Corn Yield. Avaliable online: http://corn.agronomy.wisc.edu/AA/pdfs/A033.pdf. (Accessed 3 July 2018).

Lee, K., & Lee, B. (2013). Estimation of rice growth and nitrogen nutrition status using color digital camera image analysis. *European Journal of Agronomy, 48*, 57–65. https://doi.org/10.1016/j.eja.2013.02.011.

Maimaitijiang, M., Ghulam, A., Sidike, P., Hartling, S., Maimaitiyiming, M., Peterson, K., et al. (2017). Unmanned Aerial System (UAS)-based phenotyping of soybean using multi-sensor data fusion and extreme learning machine. *ISPRS Journal of Photogrammetry and Remote Sensing, 134*, 43–58. https://doi.org/10.1016/j.isprsjprs.2017.10.011.

Malambo, L., Popescu, S. C., Murray, S. C., Putman, E., Pugh, N. A., Horne, D. W., et al. (2018). Multitemporal field-based plant height estimation using 3D point clouds generated from small unmanned aerial systems high-resolution imagery. *International Journal of Applied Earth Observation and Geoinformation, 64*, 31–42. https://doi.org/10.1016/j.jag.2017.08.014.

Mangus, D. L., Sharda, A., & Zhang, N. (2016). Development and evaluation of thermal infrared imaging system for high spatial and temporal resolution crop water stress monitoring of corn within a greenhouse. *Computers and Electronics in Agriculture, 121*, 149–159. https://doi.org/10.1016/j.compag.2015.12.007.

MarketsandMarkets. (2013). *Unmanned aerial vehicle market (2013–2018)*. Dallas, TX, USA: Technical Report. MarketsandMarkets.

Martin, B. R. (2012). *Statistics for physical science*. Boston: Academic Press (Chapter 8).

Meyer, G. E., & Neto, C. J. (2008). Verification of color vegetation indices for automated crop imaging applications. *Computers and Electronics in Agriculture, 63*, 282–293.

Mohammed, N. Z., Ghazi, A., & Mustafa, H. E. (2013). Positional accuracy testing of google earth. *International Journal of Multidisciplinary Sciences and Engineering, 4*(6), 6–9.

Nebiker, S., Lack, N., Abächerli, M., & Läderach, S. (2016). Light-weight multispectral uav sensors and their capabilities for predicting grain yield and detecting plant diseases. *ISPRS - International Archives of the Photogrammetry, Remote Sensing and Spatial Information Sciences, XLI-B1*, 963–970. https://doi.org/10.5194/isprsarchives-XLI-B1-963-2016.

Panda, S. S., Panigrahi, S., & Ames, D. P. (2010). Crop yield forecasting from remotely sensed aerial images with self-organizing maps. *Transactions of ASABE, 53*(2), 323–338.

Pantazi, X. E., Moshou, D., Alexandridis, T., Whetton, R. L., & Mouazen, A. M. (2016). Wheat yield prediction using machine learning and advanced sensing techniques. *Computers and Electronics in Agriculture, 121*, 57–65. https://doi.org/10.1016/j.compag.2015.11.018.

Sepulcre-Cantó, G., Zarco-Tejada, P. J., Jiménez-Muñoz, J. C., Sobrino, J. A., Miguel, E.d., & Villalobos, F. J. (2006). Detection of water stress in an olive orchard with thermal remote sensing imagery. *Agricultural and Forest Meteorology, 136*(1–2), 31–44. https://doi.org/10.1016/j.agrformet.2006.01.008.

Shukla, A. K., Ladha, J. K., Singh, V. K., Dwivedi, B. S., Balasubramanian, V., Gupta, R. K., et al. (2004). Calibrating the leaf color chart for nitrogen management in different genotypes of rice and wheat in a systems perspective. *Agronomy Journal, 96*(6), 1606–1621. https://doi.org/10.2134/agronj2004.1606.

Stevens, G., Motavalli, P., Scharf, P., Nathan, M., & Dunn, D. (2002). Crop nutrient deficiencies and toxicities. http://muextension.missouri.edu/xplor/agguides/pests/ipm1016.html.

Sudduth, K. A., Drummond, S. T., & Kitchen, N. R. (2015). *Operational characteristics of commercial crop canopy sensors for nitrogen application in maize Precision agriculture* (Vol. 15, pp. 51–58). Wageningen Academic Publishers.

Sudduth, K. A., Drummond, S. T., & Myers, D. B. (2012). In *Yield editor 2.0: Software for automated removal of yield map errors, 2012 Dallas, Texas, July 29August* (Vol. 1, p. 2012). https://www.ars.usda.gov/research/software/download/?softwareid=370.

Turner, D., Lucieer, A., Malenovský, Z., King, H. D., & Robinson, A. S. (2014). Spatial co-registration of ultra-high resolution visible, multispectral and thermal images acquired with a Micro-UAV over Antarctic moss beds. *Remote Sensing, 6*(5). https://doi.org/10.3390/rs6054003.

USDA-NRCS. (2000). *Major land resource areas*. Washington, D.C: USDA-Natural Resources Conservation Service.

Vega, F. A., Ramírez, F. C., Saiz, M. P., & Rosúa, F. O. (2015). Multi-temporal imaging using an unmanned aerial vehicle for monitoring a sunflower crop. *Biosystems Engineering, 132*, 19–27. https://doi.org/10.1016/j.biosystemseng.2015.01.008.

Wang, J., Li, X., Lu, L., & Fang, F. (2013). Estimating near future regional corn yields by integrating multi-source observations into a crop growth model. *European Journal of Agronomy, 49*, 126–140. https://doi.org/10.1016/j.eja.2013.03.005.

Woebbecke, D. M., Meyer, G. E., Vonbargen, K., & Mortensen, D. A. (1995). Color indices for weed identification under various soil, residue, and lighting conditions. *Transactions Of the ASAE, 38*(1), 259–269.

Xue, H., Han, Y., Li, Y., Wang, G., Feng, L., Fan, Z., et al. (2017). Estimating light interception using the color attributes of digital images of cotton canopies. *Journal of Integrative Agriculture, 16*(7), 1474–1485. https://doi.org/10.1016/S2095-3119(16)61542-3.

Xue, J., & Su, B. (2017). Significant remote sensing vegetation indices: A review of developments and applications. *Journal of Sensors, 2017*, 1–17. https://doi.org/10.1155/2017/1353691.

Yang, W., Wang, S., Zhao, X., Zhang, J., & Feng, J. (2015). Greenness identification based on HSV decision tree. *Information Processing in Agriculture, 2*(3), 149–160. https://doi.org/10.1016/j.inpa.2015.07.003.

Yin, X., Jaja, N., McClure, M. A., & Hayes, M. R. (2011). Comparison of models in assessing relationship of corn yield with plant height measured during early- to mid-season. *Journal of Agricultural Science, 3*(3). https://doi.org/10.5539/jas.v3n3p14.

Zhang, C., & Kovacs, J. M. (2012). The application of small unmanned aerial systems for precision agriculture: A review. *Precision Agriculture, 13*(6), 693–712. https://doi.org/10.1007/s11119-012-9274-5.

Zhang, M., Qin, Z., Liu, X., & Ustin, S. L. (2003). Detection of stress in tomatoes induced by late blight disease in California, USA, using hyperspectral remote sensing. *International Journal of Applied Earth Observation and Geoinformation, 4*(4), 295–310. https://doi.org/10.1016/S0303-2434(03)00008-4.

Zheng, Y., Zhu, Q., Huang, M., Guo, Y., & Qin, J. (2017). Maize and weed classification using color indices with support vector data description in outdoor fields. *Computers and Electronics in Agriculture, 141*, 215–222. https://doi.org/10.1016/j.compag.2017.07.028.

Zhou, R., Damerow, L., Sun, Y., & Blanke, M. M. (2012). Using colour features of cv. 'Gala' apple fruits in an orchard in image processing to predict yield. *Precision Agriculture, 13*(5), 568–580. https://doi.org/10.1007/s11119-012-9269-2.

Łuszczkiewicz-Piątek, M. (2014). Which color space should be chosen for robust color image retrieval based on mixture modeling. In S. Choras R (Ed.), *Image processing and communications challenges 5. Advances in intelligent systems and computing* (Vol. 233). Heidelberg: Springer.